New Journal of Physics
The open access journal at the forefront of physics

Deutsche Physikalische Gesellschaft DPG IOP Institute of Physics

PAPER • OPEN ACCESS

Evanescent-field assisted photon collection from quantum emitters under a solid immersion lens

To cite this article: S G Bishop *et al* 2022 *New J. Phys.* **24** 103027

New Journal of Physics
The open access journal at the forefront of physics

Deutsche Physikalische Gesellschaft DPG
IOP Institute of Physics

Published in partnership with: Deutsche Physikalische Gesellschaft and the Institute of Physics

OPEN ACCESS

RECEIVED
17 June 2022

REVISED
27 September 2022

ACCEPTED FOR PUBLICATION
30 September 2022

PUBLISHED
21 October 2022

PAPER

Evanescent-field assisted photon collection from quantum emitters under a solid immersion lens

S G Bishop[1,2], J K Cannon[1,2], H B Yağci[1,2], R N Clark[1,2], J P Hadden[1,2], W Langbein[3] and A J Bennett[1,2,3,*]

[1] School of Engineering, Cardiff University, Queen's Building, The Parade, Cardiff, CF24 3AA, United Kingdom
[2] Translational Research Hub, Cardiff University, Maindy Road, Cathays, Cardiff, CF24 4HQ, United Kingdom
[3] School of Physics and Astronomy, Cardiff University, Queen's Building, The Parade, Cardiff, CF24 3AA, United Kingdom
[*] Author to whom any correspondence should be addressed.

E-mail: BennettA19@cardiff.ac.uk

Keywords: single photon source, solid immersion lens, III-nitride, aluminium nitride, quantum optics, quantum photonics, colour centre

Supplementary material for this article is available online

Abstract

Solid-state quantum light sources are being intensively investigated for applications in quantum technology. A key challenge is to extract light from host materials with high refractive index, where efficiency is limited by refraction and total internal reflection. Here we show that an index-matched solid immersion lens can, if placed sufficiently close to the semiconductor, extract light coupled through the evanescent field at the surface. Using both numerical simulations and experiments, we investigate how changing the thickness of the spacer between the semiconductor and lens impacts the collection efficiency (CE). Using automatic selection and measurement of 100 s of individually addressable colour centres in several aluminium nitride samples we demonstrate spacer-thickness dependent photon CE enhancement, with a mean enhancement factor of 4.2 and a highest measured photon detection rate of 743 ± 4kcps.

1. Introduction

The number of photons collected from a source is of paramount importance for any quantum optoelectronic technology. This is especially critical for quantum light sources such as colour centres, quantum dots and single ions where increasing the photon flux is necessary to allow measurement of correlation effects. However, in solid state systems these emitters are embedded in high refractive index materials such as diamond (index 2.41 at 600 nm), gallium arsenide (3.87), silicon carbide (2.70) or indium phosphide (3.57). Refraction at the air-dielectric surface reduces the solid angle over which light may be collected inside the material. At high emission angles, light is lost at the interface due to total internal reflection (TIR), placing an upper limit on the efficiency. Various micro-processed architectures have been demonstrated to increase collection efficiency (CE), including etched micro-pillars [1, 2], nanowire antennae [3, 4], photonic crystals [5, 6], dielectric resonators [7, 8], and free-space cavities [9, 10]. All require the photonic structure to be aligned to the emitter in space and frequency, which does not easily support the study of randomly positioned, broadband emitters. In contrast, a millimeter-sized solid immersion lens (SIL) [11–13], a dielectric half-sphere, offers an inherently wide-field CE enhancement over a broad spectral range. This enhancement is optimised for buried emitters when the refractive index of the SIL is matched to the index of the semiconductor [14, 15].

Quantum dots in gallium nitride (GaN) are unique in offering quantum light emission in the blue and UV part of the spectrum [16]. Due to the recent discovery of quantum emitters in GaN [17, 18] and aluminium nitride (AlN) [19], there is renewed interest in nitrides as a platform for quantum optics in the visible and near infra-red. Polarised quantum light emission at room temperature, coupled with established processing technology, presents an exciting platform combining optoelectronic components, integrated

photonics, and quantum emitters [20]. In addition, GaN presents one of the only known room temperature quantum emitters in the telecom band [18].

In this report, we demonstrate how a SIL enhances the CE from colour centres in AlN [19]. We use confocal microscopy with an index matched ZrO_2 hemispherical SIL (h-SIL) ($n_{SIL} = 2.16$ at 600 nm) on AlN templates ($n_{AlN} = 2.15$ at 600 nm). We engineer the thickness of a layer of PMMA ($n_{PMMA} = 1.49$ at 600 nm) to avoid the formation of an air gap between the semiconductor and SIL. Using finite difference time domain (FDTD) simulations, we show that engineering the thickness of the polymer is important for increasing the CE with a high numerical aperture (NA) lens due to evanescent coupling through the PMMA layer.

2. Methods

2.1. An ideal hemispherical SIL

The h-SIL, a truncated sphere bisected across its origin, exploits the SIL's geometry to increase photon CE by limiting refraction at the semiconductor-SIL interface by reducing the index difference. Additionally, aplanatic imaging is achieved due to the normal incidence of light at the SIL-air interface as shown in figure 1(a). The NA of the imaging system is therefore increased by the refractive index within the semiconductor, reducing the axial and lateral size of both the excitation and collection point-spread functions by a factor of the SIL refractive index and the square of the index, respectively, relative to imaging through a flat interface [21].

The CE may be analytically estimated from Barnes *et al* [14] considering a dipole orientated in the plane of an infinite AlN slab [19]. The blue and green plots with filled symbols in figure 1(b) demonstrate the analytically determined CE without and with a ZrO_2 SIL, respectively. The dispersion of the AlN refractive index is included in the analytically determined CE. The reflection at the SIL-air interface is accounted for with Fresnel equations, with a reflectivity of 13% at normal incidence. To take into account the effect of other reflections, such as that from the AlN to sapphire interface, which are not included in the analytical analysis, we perform FDTD simulations in Lumerical FDTD [22]. We simulate the AlN layer surrounded by a sapphire substrate ($n = 1.77$ at 600 nm) and a homogeneous ZrO_2 SIL using outgoing boundary conditions (perfectly matched layers). Anti-symmetric and symmetric boundary conditions are used across the dipole to reduce the simulated region. The loss due to the reflection at the SIL-air interface is included separately. The FDTD simulation predicts a wavelength-varying and enhanced CE with regards to the analytically determined value, due to the finite reflection from the AlN-sapphire interface, shown as the blue and green lines in figure 1(b) with empty symbols. This is evident from the electric field cross-section plots through the dipole in figures 1(c) and (d). In this scenario, the expected enhancement of light collection into a NA of 0.9 is increased by a factor of approximately 8 by the SIL, to a mean value of 35% across the visible spectrum.

2.2. Ensemble scanning

To experimentally quantify the enhancement in CE, we use a statistical analysis over an ensemble of individually addressable emitters. To reduce bias in the selection of the emitters, we developed an automated routine to locate and characterise emitters. Initially, confocal sample maps were measured revealing the presence of emitters in the AlN epilayer using an optical dual-axis 4f scanning system. Detailed information regarding the microscope used for the optical measurements, including information about the AlN sample, can be found in the supplementary material. Optical filtering was used to measure only the 550 to 650 nm spectral range, suppressing fluorescence from chromium impurities in the sapphire substrate. Due to the linearly polarised nature of the excitation laser at 532 nm and the fact that each emitter has a linearly-polarised excitation dipole with unknown orientation [19], three scan maps were taken with the laser's linear polarisation angle at 0°, 60° and 120°, shown in figures 2(a)–(c). We combine these scan maps in (d), which is the mean of scans (a)–(c), to avoid pre-selecting emitters aligned to the laser polarisation. As reported in our previous work, AlN colour centres in this samples have a zero-phonon line at 595 nm with a broad phonon side-band extending to 700 nm [19].

The resultant scan map was then fed into an algorithm that locates emitters in the following manner. Initially, the algorithm removes single pixel noise by using a 3×3 pixel median filter and further smooths the image by convolving the image with a two-dimensional Gaussian function. A fast pixel-by-pixel analysis then locates potential emitter locations based on the intensity of neighbouring pixels. The 126 candidate emitter locations are marked in figure 2(e). It can be observed in the image that the algorithm overestimates the number of emitters and occasionally selects features smaller than the diffraction limited lateral spot size. Therefore, a two-dimensional Gaussian function is fit to each emitter. The Gaussian fit parameters are also used to rank the emitters based on the Gaussian width being close to the expected diffraction limited

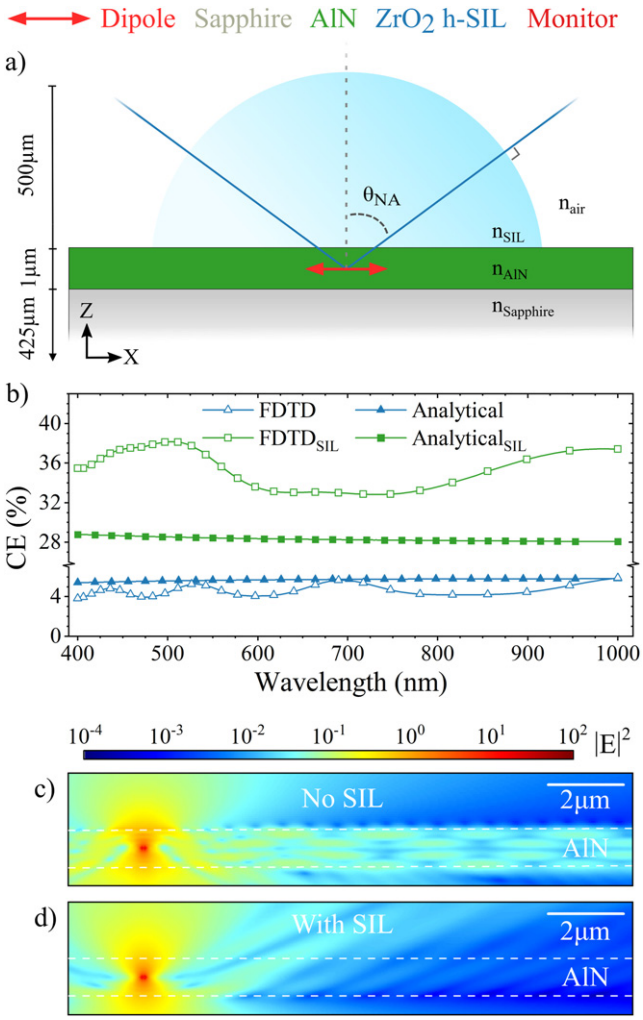

Figure 1. The hemispherical SIL. (a) Illustration of the geometry. (b) Calculated (filled symbols) and simulated (empty symbols) CE as a function of the wavelength of the dipole with (green) and without (blue) a h-SIL. (c) and (d) *XZ* slices of the log of the electric field across the dipole without and with the SIL respectively.

point-spread function of the microscope, symmetry in X and Y, amplitude and goodness of fit R^2 value. This Gaussian fit identifies the centre of the emitters' point spread function with greater precision than the scan step-size. Post filtering, 92 emitters are identified in the scan map figure 2(f).

Power dependent saturation measurements are then taken on each candidate emitter sequentially using the following automated process. Firstly, the scanning system moves to the approximate emitter location. X, Y and Z line scans are performed to find the maximum along each axis. The linear polarisation of the 532 nm excitation laser is rotated to maximally couple to the emitter's absorption dipole. Then a laser-power P dependent intensity $I(P)$ was measured and used to quantify the fitted saturation intensity at infinite power I_∞ as defined by the fit function $I(P) = I_\infty P/(P + P_{\text{sat}})$. Measurements with a saturation power greater than 2 mW are removed from each data-set as this is a good proxy for linear power dependent behaviour, which is not consistent with a single colour centre (this occurs with less than 5% frequency). No polarisation optics were included in the collection path of our microscope. Throughout the measurements, photo-bleaching was not observed for any emitters but random telegraph noise in the detected count rate is common.

3. Results and discussion

3.1. Collection efficiency enhancement

Using the automated system we set out to determine the efficiency enhancement for an ensemble of emitters under a SIL. We emphasise that the presence of an air-gap between the SIL and AlN suppresses such an enhancement. An air gap can arise from a non-flat back surface of the SIL and/or a non-flat surface of the semiconductor. To prevent such a gap, we add a thin layer of a polymer, PMMA, which is soft enough to fill

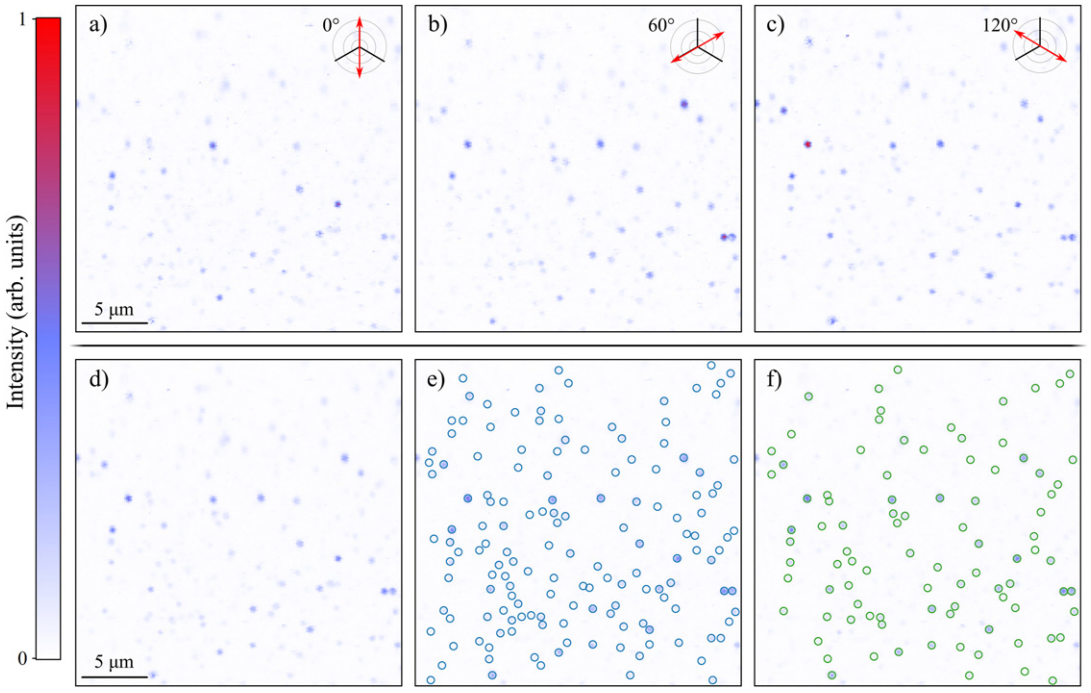

Figure 2. Automated selection of emitters in confocal scan maps. (a)–(c) Excitation polarisation resolved confocal scans, where the excitation laser polarisation is rotated in the plane of the sample at an angle of 0°(a), 60°(b) and 120°(c) respectively. (d) Combined scan map where each pixel represents the mean of the 3 polarisation resolved scan maps. (e) Emitter locations determined with the fast peak finding technique. (f) Corresponding filtered emitter locations after Gaussian fitting to each emitter's point-spread function.

the gap between the SIL and AlN adapting to their surfaces, in line with other reports [12, 21]. Three samples of AlN-on-sapphire from the same wafer were studied. One with no SIL (SP1), one with 212 nm of PMMA between the SIL and AlN (SP2) and one with 70 nm of PMMA (SP3). The PMMA thickness was determined using an ellipsometer prior to the addition of the SIL.

The statistical distribution of emitter saturation intensities in each sample is presented in figure 3. In sample SP1, without the SIL, 396 emitters were measured and the resulting distribution is shown in figure 3(a). The mean of the distribution is given as $\mu_{SP1} = 68$ kcps. Although a similar mean intensity to the NV centre in diamond, the variance in the saturation intensities differs significantly to what is seen in the NV centre in diamond where a narrow distribution is often reported [3], which can be correlated with the NV orientation. We attribute the larger variation in emitter brightness to differences in the internal energy levels between emitters which periodically suppress emission on different timescales. For example, a metastable shelving state [19] evident in the photon statistics of nearly all emitters, leads to pump power dependent bunching of emission on timescales of tens to hundreds of nanoseconds. Additionally, some emitters show telegraph noise which is observed on timescales of seconds, but may also be present on millisecond or microsecond scales. The relationship between these instabilities and the time-averaged intensity will be the subject of a future study. However, it is notable that the predicted photon CE should lead to a saturated emission intensity at least an order of magnitude greater than we measure, based on the extrapolated zero-pump power lifetime $t_1 = 4.6$ ns as determined from fitting the second order correlation measurements in figure 3(f).

In SP1, 396 emitters were sampled over an area of 150 μm by 150 μm, corresponding to an area of 57 μm^2 per emitter. Due to the magnification of the SIL, where the displacement in X and Y of our imaging system leads to a displacement of X/n_{SIL} and Y/n_{SIL} on the sample surface respectively, we ensure we sample a similar number of emitters per unit area scanned for SP2 and SP3. 63 and 70 emitters are measured for SP2 and SP3 respectively, with the corresponding distribution in I_∞ shown in in figures 3(b) and (c).

The mean μ of the saturated intensity I_∞ distribution in each sample is shown as the dashed vertical lines in figure 3(a)–(c). For SP2 and SP3, the mean I_∞ is 211 and 285 kcps, respectively. This corresponds to an enhancement factor of 3.1 and 4.2, relative to SP1. Assuming that the mean of the distribution for SP1 represents a CE of 4.6%, as determined from the analytical analysis, the projected CE for SP2 and SP3 can be estimated to be 14.3% and 19.3%. The calculated standard deviation σ increases with the introduction of the SIL (SP2) and decreasing polymer thickness (SP3). This may be attributed to the associated

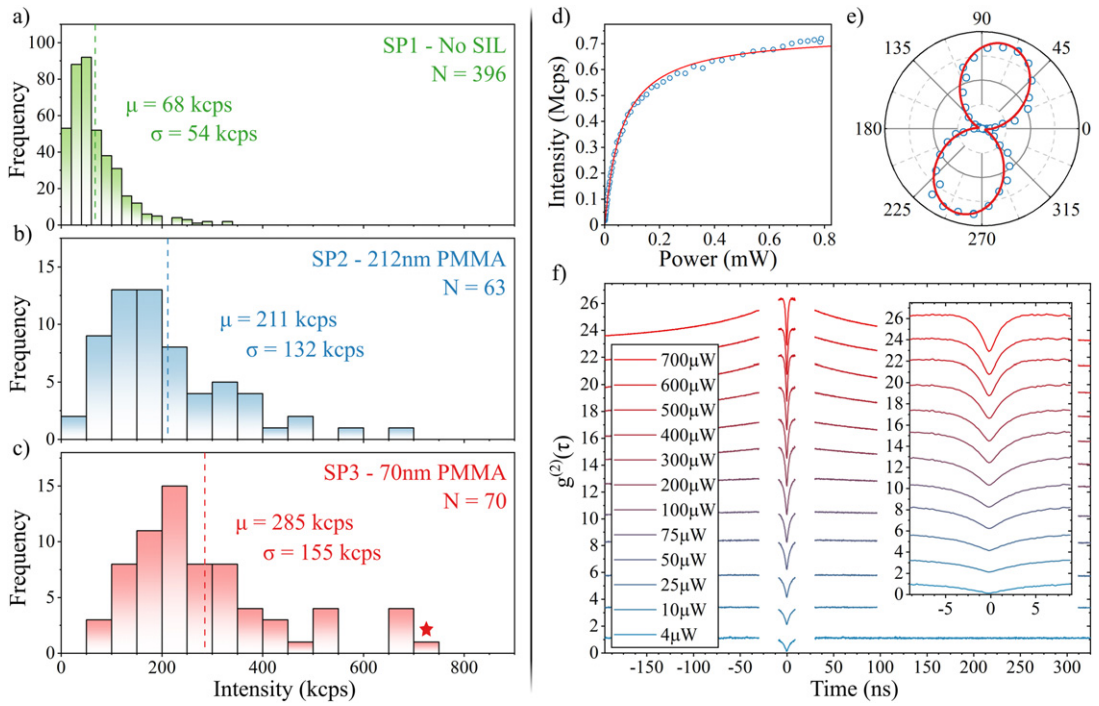

Figure 3. Evanescent-field assisted collection by a h-SIL. (a)–(c) Histogram representing the fitted saturation intensity at infinite power, I_∞, for a number of emitters in samples SP1, SP2 and SP3. The polymer thickness is labelled on each plot. For the brightest emitter in SP3 (marked with a red star) we show the power-dependent intensity saturation curve (d), the intensity as a function of excitation polarisation (e) and power dependent auto-correlation histograms (f). Each power-dependent histogram is stacked with an offset of 2 for clarity. The insert in (f) focuses on the power dependent auto-correlation data around time zero.

multiplicative enhancement in CE. We note that the highest detected count rate is measured in an emitter in SP3 with $I_\infty = 743 \pm 4$ kcps. We show data for this emitter in figure 3, labelled in (c) with a star. An absorption polarisation measurement in (e) illustrates the linear dipole absorption profile of the emitter with a polarisation angle $\theta = 73.9 \pm 0.8°$. The absorption measurement demonstrates a degree of polarisation, as defined by $\rho = (I_{max} - I_{min})/(I_{max} + I_{min}) = 0.993 \pm 0.007$. Pump power dependent auto-correlation data in (f) shows the presence of anti-bunching near time zero, in combination with longer timescale bunching at high pump powers. A fit to the 4 μW measurement, shown in the supplementary material, illustrates the single photon purity, with $g^{(2)}(0) = 0.123 \pm 0.009$. In the experimental data we have removed an artefact at 8–30 ns caused by optical cross-talk in our interferometer.

3.2. Evanescent coupling

To investigate the observed CE dependence on the polymer thickness we return to FDTD. Using the aforementioned simulation environment, the CE is determined by capturing the electric field profile from a single dipole embedded in the AlN slab on a three-dimensional box of frequency domain monitors surrounding the dipole and spanning the material stack. The near-field electric field on the *XY* monitor in the ZrO_2 layer is projected into the far field, where the flux is integrated over the solid angles of the collection optics to determine the collected power. The CE is defined as the collected power normalised by the power injected into the simulation via the single dipole.

The CE as a function of the polymer thickness d and NA of the imaging system is presented in figure 4. The simulation shows that for $d > 300$ nm the CE is constant and is well below the expected CE for an ideal system with NA = 0.9, as determined in figure 1. This is due to TIR at the AlN-PMMA interface at angles greater than 44°, limiting the effective collection NA to 0.69.

The greatest gain in CE can be made by combining a high NA lens with a thin PMMA layer. The CE for a NA of 0.9 as a function of the polymer thickness is presented in figure 4(b). We attribute the increased CE for polymer thickness less than 200 nm to evanescent coupling through the polymer for light incident at angles greater than 44 degrees. The evanescent wave in the polymer is converted back to a propagating wave at the polymer-SIL interface and collected by our imaging system, a phenomenon known as frustrated TIR [23]. The electric field in the polymer decays with the distance z away from the interface (in the absence of

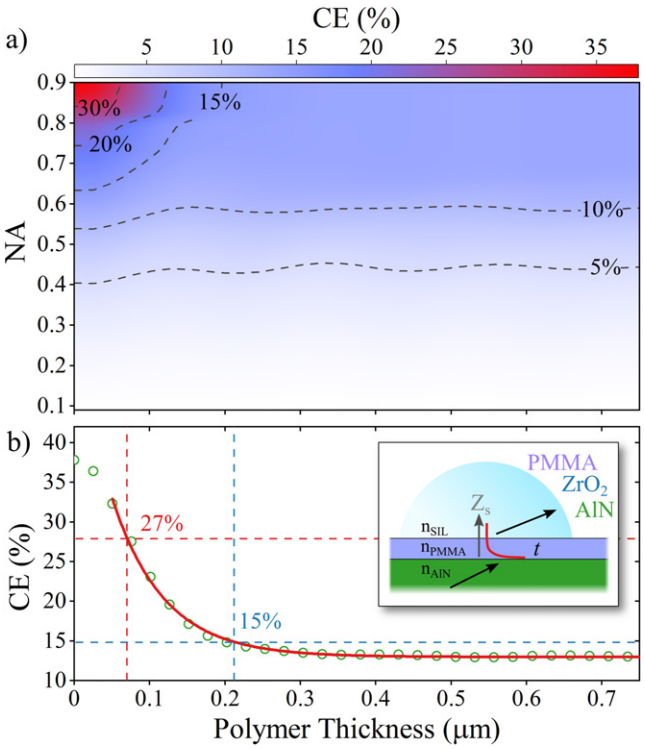

Figure 4. Simulated CE demonstrating evanescent coupling through a thin polymer layer. (a) CE as a function of the collection free space NA and the thickness d of the PMMA polymer. (b) CE as a function of the polymer thickness for NA = 0.9. The insert of (b) illustrates the coupling of the evanescent field through the polymer spacer, with a red line illustrating the exponential decay of the field's envelope.

the SIL) in the form [11],

$$E(z) = E(s)\mathrm{e}^{-z/d} \quad \text{and,} \quad p = \frac{\lambda_{\mathrm{Air}}/n_{\mathrm{AlN}}}{2\pi\sqrt{\left(\frac{n_{\mathrm{AlN}}}{n_{\mathrm{PMMA}}}\right)^2 \sin^2(\theta) - 1}} \tag{1}$$

where $E(z)$ is the electric field normal to the interface, $E(s)$ is the electric field at the surface, θ is the incidence angle of the light, λ_0 is the wavelength of the light in vacuum and p is the penetration depth of the evanescent wave.

Due to the angle dependence of the coupling through the polymer, we consider the two limiting angles of the system, just beyond the angle of TIR, $\theta_{\mathrm{TIR}} = 45°$, and the NA of the imaging system, $\theta_{\mathrm{NA}} = 65°$. The penetration depths as determined using equation (1) are given as $p_{\mathrm{TIR}} = 228$ nm and $p_{\mathrm{NA}} = 53$ nm, respectively. The determined penetration depths agree well with the simulated thickness dependent CE in figure 4, where for $d < 200$ nm the CE is increased above the vanishing value at infinite polymer thickness. A fit to the data in figure 4(b) using an exponential offset is used to interpolate the expected CE for SP2 and SP3. The determined CE values of 15 and 27% agree well with the projected values from the statistical measurements.

4. Conclusion

The photon CE of quantum emitters in a AlN-on-sapphire substrate was enhanced by engineering the thickness of a PMMA adhesion layer under a h-SIL. An automated emitter finding routine was used to determine the CE enhancement of an ensemble. We demonstrate experimentally and numerically that at high NA and low PMMA thickness evanescent coupling through the polymer can maximise CE. A CE of 19.3% is inferred for a polymer thickness of 70 nm, in good agreement with numerical simulations. The significant increase in CE from these room temperature quantum emitters is a step towards efficient off-the-shelf room temperature quantum light sources.

Acknowledgments

We acknowledge financial support provided by EPSRC via Grant No. EP/T017813/1 and the European Union's H2020 Marie Curie ITN project LasIonDef (GA No. 956387). Device processing was carried out in the cleanroom of the ERDF-funded Institute for Compound Semiconductors (ICS) at Cardiff University. We thank R Hekmati for assembling the heating stage used to adhere the SIL to the PMMA, after it was manually positioned.

Data availability statement

The data that supports the findings of this study are available upon reasonable request at http://doi.org/10.17035/d.2022.0220107749.

Conflict of interest

The authors have no conflicts to disclose.

Author contributions statement

All authors contributed to this work.

ORCID iDs

S G Bishop https://orcid.org/0000-0001-6353-6601
J K Cannon https://orcid.org/0000-0002-7860-1290
H B Yağci https://orcid.org/0000-0002-8992-2292
R N Clark https://orcid.org/0000-0002-6623-1499
J P Hadden https://orcid.org/0000-0001-5407-6754
W Langbein https://orcid.org/0000-0001-9786-1023
A J Bennett https://orcid.org/0000-0002-5386-3710

References

[1] Santori C, Fattal D, Vučković J, Solomon G S and Yamamoto Y 2002 Indistinguishable photons from a single-photon device *Nature* **419** 594–7
[2] Somaschi N *et al* 2016 Near-optimal single-photon sources in the solid state *Nat. Photon.* **10** 340–5
[3] Babinec T M, Hausmann B J, Khan M, Zhang Y, Maze J R, Hemmer P R and Lončar M 2010 A diamond nanowire single-photon source *Nat. Nanotechnol.* **5** 195–9
[4] Claudon J, Bleuse J, Malik N S, Bazin M, Jaffrennou P, Gregersen N, Sauvan C, Lalanne P and Gérard J-M 2010 A highly efficient single-photon source based on a quantum dot in a photonic nanowire *Nat. Photon.* **4** 174–7
[5] Noda S, Fujita M and Asano T 2007 Spontaneous-emission control by photonic crystals and nanocavities *Nat. Photon.* **1** 449–58
[6] Lodahl P, Mahmoodian S and Stobbe S 2015 Interfacing single photons and single quantum dots with photonic nanostructures *Rev. Mod. Phys.* **87** 347–400
[7] Kuznetsov A I, Miroshnichenko A E, Brongersma M L, Kivshar Y S and Luk'yanchuk B 2016 Optically resonant dielectric nanostructures *Science* **354** 846–55
[8] Mignuzzi S, Vezzoli S, Horsley S A, Barnes W L, Maier S A and Sapienza R 2019 Nanoscale design of the local density of optical states *Nano Lett.* **19** 1613–7
[9] Tomm N *et al* 2021 A bright and fast source of coherent single photons *Nat. Nanotechnol.* **16** 399–403
[10] Dolan P R, Hughes G M, Grazioso F, Patton B R and Smith J M 2010 Femtoliter tunable optical cavity arrays *Opt. Lett.* **35** 3556–8
[11] Born M and Wolf E 1999 *Principles of Optics: Electromagnetic Theory of Propagation, Interference and Diffraction of Light* 7th edn (Cambridge: Cambridge University Press)
[12] Vamivakas A N, Atatüre M, Dreiser J, Yilmaz S T, Badolato A, Swan A K, Goldberg B B, Imamoğlu A and Ünlü M S 2007 Strong extinction of a far-field laser beam by a single quantum dot *Nano Lett.* **7** 2892–6
[13] Chen Y, Zopf M, Keil R, Ding F and Schmidt O G 2018 Highly-efficient extraction of entangled photons from quantum dots using a broadband optical antenna *Nat. Commun.* **9** 2994
[14] Barnes W L, Björk G, Gérard J M, Jonsson P, Wasey J A, Worthing P T and Zwiller V 2002 Solid-state single photon sources: light collection strategies *Eur. Phys. J.* D **18** 197–210
[15] Laiho K, Dirmeier T, Schmidt M, Reitzenstein S and Marquardt C 2022 Measuring higher-order photon correlations of faint quantum light: a short review *Phys. Lett.* A **435** 021854
[16] Zhu T and Oliver R A 2016 Nitride quantum light sources *Europhys. Lett.* **113** 38001
[17] Berhane A M *et al* 2017 Bright room-temperature single-photon emission from defects in gallium nitride *Adv. Mater.* **29** 1605092
[18] Zhou Y *et al* 2018 Room temperature solid-state quantum emitters in the telecom range *Sci. Adv.* **4** eaar3580

[19] Bishop S G, Hadden J P, Alzahrani F D, Hekmati R, Huffaker D L, Langbein W W and Bennett A J 2020 Room-temperature quantum emitter in aluminum nitride *ACS Photonics* **7** 1636–41
[20] Wan N H *et al* 2020 Large-scale integration of artificial atoms in hybrid photonic circuits *Nature* **583** 226–31
[21] Bishop S G, Hadden J P, Hekmati R, Cannon J K, Langbein W W and Bennett A J 2022 Enhanced light collection from a gallium nitride color center using a near index-matched solid immersion lens *Appl. Phys. Lett.* **120** 114001
[22] Lumerical Inc. 2021 https://optics.ansys.com/hc/en-us/articles/1500007184901-Lumerical-Citation-Instruction
[23] Zhu S, Yu A W, Hawley D and Roy R 1986 Frustrated total internal reflection: a demonstration and review *Am. J. Phys.* **54** 601–7